Debonding of coin-shaped osseointegrated implants: Coupling of experimental and numerical approaches

Yoann Hériveaux, Sophie Le Cann, Katharina Immel, Elsa Vennat, Vu-Hieu Nguyen, Vladimir Brailovski, Patrick Karasinski, Roger A Sauer, Guillaume Haiat

Debonding of coin-shaped osseointegrated implants: coupling of experimental and numerical approaches

Yoann Hériveaux[1], Sophie Le Cann[2], Katharina Immel[2,3], Elsa Vennat[1], Vu-Hieu Nguyen[4], Vladimir Brailovski[5], Patrick Karasinski[6], Roger A. Sauer[7,8,9], Guillaume Haïat[2]*

1. Université Paris-Saclay, CentraleSupélec, ENS Paris-Saclay, CNRS, LMPS - Laboratoire de Mécanique Paris-Saclay, 91190, Gif-sur-Yvette, France.

2. CNRS, Univ Paris Est Creteil, Univ Gustave Eiffel, UMR 8208, MSME, F-94010 Créteil, France

3. Aachen Institute for Advanced Study in Computational Engineering Science, RWTH Aachen University, Germany;

4. Univ Paris Est Creteil, Univ Gustave Eiffel, CNRS, UMR 8208, MSME, F-94010 Créteil, France

5. Department of Mechanical Engineering, École de technologie supérieure, 1100 Notre-Dame Street West, Montreal, QC H3C 1K3, Canada;

6. Université Paris-Est, Laboratoire Images, Signaux et Systèmes Intelligents – EA 3956, 61 avenue du Général de Gaulle, 94010 Créteil Cedex, France.

7. Faculty of Civil and Environmental Engineering, Gdansk University of Technology, Poland;

8. Aachen Institute for Advanced Study in Computational Engineering Science, RWTH Aachen University, Germany;

9. Dept. of Mechanical Engineering, Indian Institute of Technology Guwahati, Assam, India.

*Corresponding author:
Laboratoire Modélisation Simulation Multi-Échelle, UMR CNRS 8208,
61 avenue du général de Gaulle, 94010 Créteil, France
e-mail : guillaume.haiat@cnrs.fr

To appear in: Journal of the Mechanical Behavior of Biomedical Material
DOI: https://doi.org/10.1016/j.jmbbm.2023.105787
Reference: JMBBM 105787

Abstract

While cementless implants are now widely used clinically, implant debonding still occur and is difficult to anticipate. Assessing the biomechanical strength of the bone–implant interface can help improving the understanding of osseointegration phenomena and thus preventing surgical failures. A dedicated and standardized implant model was considered. The samples were tested using a mode III cleavage device to assess the mechanical strength of the bone-implant interface by combining experimental and numerical approaches. Four rough (*Sa* = 24.5 µm) osseointegrated coin-shaped implants were left in sheep cortical bone during 15 weeks of healing time. Each sample was experimentally rotated at 0.03°/sec until complete rupture of the interface. The maximum values of the torque were comprised between 0.48 and 0.72 N.m, while a significant increase of the normal force from 7-12 N to 31-43 N was observed during the bone-implant interface debonding, suggesting the generation of bone debris at the bone-implant interface. The experimental results were compared to an isogeometric finite element model describing the adhesion and debonding phenomena through a modified Coulomb's law, based on a varying friction coefficient to represent the transition from an unbroken to a broken bone-implant interface. A good agreement was found between numerical and experimental torques, with numerical friction coefficients decreasing from 8.93 to 1.23 during the bone-implant interface rupture, which constitutes a validation of this model to simulate the debonding of an osseointegrated bone-implant interface subjected to torsion.

Keywords: bone-implant interface; friction; adhesion; osseointegration; finite element modeling

I. Introduction

Endosseous, cementless implants are widely used in the clinic. However, implant failures still occur and are difficult to anticipate, since the evolution of the biomechanical properties of the bone-implant interface remains only partially understood (Haïat et al., 2014; Mathieu et al., 2014). The clinical success depends on the mechanical strength of the bone-implant interface (de Vries et al., 2022; Shirazi-Adl et al., 1993), which is determined by adhesion and friction phenomena.

Pull-out tests have been carried out to evaluate the degree of bone attachment to the implant (Berahmani et al., 2017; Oliscovicz et al., 2013; Seong et al., 2013). However, the results are influenced by the implant geometry, which may induce complex multiaxial stress distributions (Shirazi-Adl, 1992) and unstable crack propagation. The mechanical strength of an interface can only be assessed under steady-state conditions of crack propagation. To standardize the measurements, coin-shaped implants with a planar bone-implant interface have been developed in the literature (Rønold et al., 2003; Rønold and Ellingsen, 2002). Although such model is different from implants employed in the clinics, it has the advantage of standardizing the measurements and allowing a steady-state debonding configuration, which is the only solution to assess the mechanical stress of the bone-implant interface. Note that such implant model has also been used because i) the planar interface allows the study of the ultrasonic response of the bone-implant interface in a simple configuration (Fraulob et al., 2020; Mathieu et al., 2012b) and ii) the possibility to add a bone chamber enables the clear distinction between mature and newly-formed bone tissues, which is interesting to study the biomechanical properties of the bone-implant interface at the micrometer scale (Guillaume et al., 2021).

Such implant model has been used in a mechanical testing device considering a mode III crack propagation (Mathieu et al., 2012a), which corresponds to a stable crack propagation compared to the pull-out tests (Seong et al., 2013). This mode III debonding analysis allows the investigation of the frictional and adhesive behavior of the bone-implant interface (Chateauminois et al., 2010) and is of clinical interest since this failure mode may occur in many clinical situations. However, the normal force at the bone-implant interface was not recorded in (Mathieu et al., 2012a), which did not allow to fully investigate the tribological behavior of the bone-implant interface nor the balance between adhesion and friction phenomena. Another limitation of (Mathieu et al., 2012a) was that the analytical stiction model was not able to accurately predict the mechanical behavior of the debonding bone-implant interface. Instead, an energetic approach was considered to assess the stress intensity factor.

While most numerical studies modeling the biomechanical behavior of the bone-implant system in the literature either considered a fully-bonded bone-implant interface (Kurniawan et al., 2012), frictionless contact (Galloway et al., 2013) or pure Coulomb's friction (I-Chiang et al., 2014; Mondal and Ghosh, 2019), such assumptions cannot accurately describe the tribological behavior of an osseointegrated bone-implant interface (Tschegg et al., 2011) because adhesion phenomena are not taken into account. Interestingly, a recent study by our group (Immel et al., 2020) developed an isogeometric numerical model describing the frictional and adhesive contact behavior of debonding and osseointegrated implants. The coupling of adhesion and friction phenomena at the bone-implant interface was modeled using a state variable friction law derived from (Rice and Ruina, 1983; Ruina, 1983). A first experimental validation of the model was performed using the results obtained in (Mathieu et al., 2012a), but this validation was limited due to the reduced number of samples and to the absence of data on compressive stresses at the bone-implant interface.

The present study aims at investigating the mechanical behavior of an osseointegrated bone-implant interface submitted to torsional loading, by combining an experimental approach with an isogeometric numerical method. The specific objective is to provide quantitative data related to the mechanical strength of the bone-implant interface that can be used in future studies to model the bone-implant interface debonding. Four coin-shaped implants osseointegrated in sheep bone for 15 weeks were debonded from the host bone through a mode III cleavage test. The variations of the normal force and of the torque were recorded and the results were compared to a numerical model (Immel et al., 2020), in order to study the phenomena occurring during the mechanical debonding of the bone-implant interface.

II. Material and methods

A. Implants and surgical procedure

Four coin-shaped implants (Ø5 mm, 3 mm thickness, named with letters A to D) made of Ti6Al4V were obtained through 3D-printing (EOS M280, EOS, Germany), displaying an average arithmetic roughness *Sa* = 24.5 +/- 6.5 µm, as measured using a tribological device. Two implants were placed on the lateral side of each left tarsi diaphysis of two 3 years old, female Préalpes sheep. The surgical procedure was described in (Vayron et al., 2018). Briefly, the implantation site was exposed to drill a Ø5.6 mm planar cavity into the cortical bone. Irrigation holes allowed fluid flow from the medullary canal towards the interface. Polytetrafluoroethylene (PTFE) caps were placed around the implants to prevent bone growth around the implant. The implants were secured in contact with the bone thanks to four Ø1.6 mm osteosynthesis screws (Easy Implant, Chavanod, France) linked by orthodontic rubber ties. The animals were housed at the École Nationale Vétérinaire d'Alfort (ENVA) in accordance with the requirements of the European Guidelines for care and use of laboratory animals and the ethical committee. After sacrifice, the samples were cleared from surrounding tissues and conserved in absolute ethanol at 4°C before testing (Fig 1A).

B. Experimental torsion of osseointegrated specimens

A mode III cleavage test was performed with the four specimens using a dedicated device (Fig. 1B) upgraded from a former experimental setup described in (Mathieu et al., 2012a). The bone was embedded into a low-shrinkage polyurethane resin (Smooth-Cast 305, Smooth-On, USA) and the implant was fixed in a home-made wrench. The rotation axes of the torque meter and of the rotation stage were carefully aligned, with a tolerance of around 100 µm. The axis of the rotation stage and of the normal of the upper wrench were aligned with an error lower than 0.1°. After 1 hour of hardening time, the bone-implant interface was progressively debonded by applying a rotation of the bone sample compared to the implant with an angular velocity of 0.03°/sec using a rotation stage (M062PD, Physik Instruments, France) until 20°. The torque (static torque meter CS 1213B, MEAS-France, France) and the normal force (load cell 85041, Burster, Germany) were recorded throughout the test, using an electronic sensor interface (9205, Burster, Germany).

After testing, the debonded implant surface was colored with van Gieson's stain to quantify the mineralized tissues with optical microscopy (Stemi 305, Zeiss, Germany). The images were threshold-based segmented using ImageJ (NIH, USA) and the BoneJ plugin to quantify the amount of bone remaining in contact with the implant, which allowed to quantify the bone-implant contact (BIC) ratio.

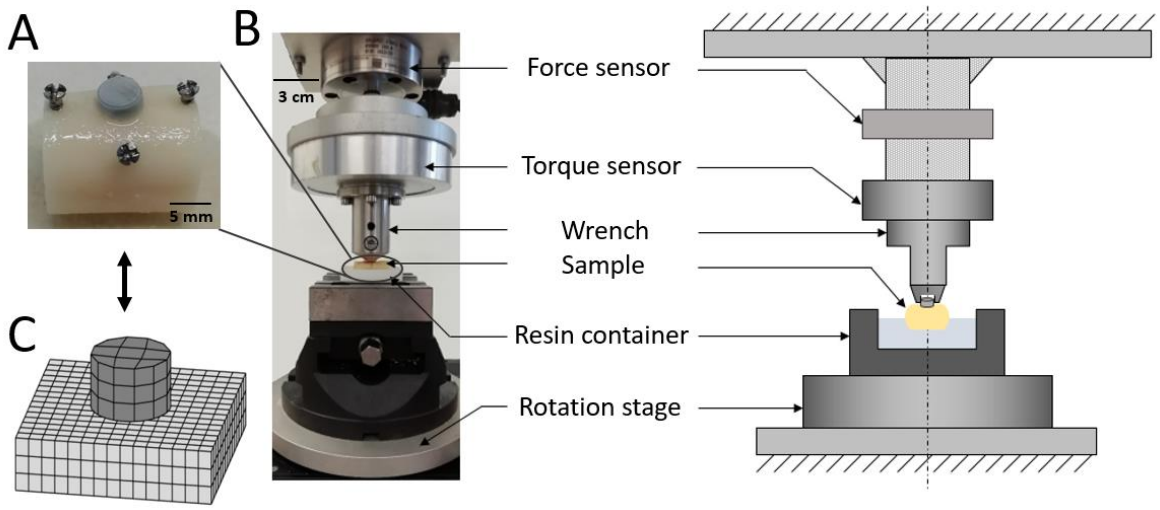

Fig. 1: Typical bone-implant specimen (A). Schematic representation and photography of the mode III cleavage test device (B). Finite element mesh of the isogeometric numerical model (C).

C. Friction tests

A non-implanted 3D-printed implant similar to the one implanted *in vivo* was tested in friction against a sheep tarsus cortical bone sample using the same device (Fig. 1B) to study the influence of the implant osseointegration on the strength of the bone-implant interface. Five friction tests were performed at a compression force around 25 N, after 30 min of relaxation time, rotating the bone with an angular velocity of 0.03°/s for 20°. The friction coefficient μ was calculated for angles between 4° and 20°, following:

$$\mu = \frac{3}{2}\frac{T}{FR} \qquad \textbf{(Eq. 1)}$$

where F is the normal force, T the torque applied between the implant and the bone sample and R the radius of the coin-shaped implant.

D. Numerical model

The torque variation during the cleavage tests was simulated using an isogeometric finite element model previously developed by our group (Immel et al., 2020). Briefly, the debonding of the bone-implant interface was modeled *via* a varying friction coefficient that controls the transition from an unbroken state, which denotes an intact osseointegrated interface, to a broken state, corresponding to pure frictional contact conditions. All simulations were performed with an in-house, MATLAB-based solver (R2018b, The MathWorks, USA).

A coin-shaped implant (Ø5 mm, 3 mm thickness) was positioned in contact with a rectangular bone cuboid (12.5 × 12.5 × 15 mm) (Fig. 1C), whose lower surface was fixed in all directions, while its sides were fixed in their corresponding normal directions. The implant and the bone bulks were discretized with linear Lagrangian shape functions with 27 and 675 elements, respectively, based on linear Lagrange shape functions, while the contact surfaces were discretized with surface elements based on quadratic NURBS shape functions. The reader is referred to (Immel et al., 2020) for the convergence study regarding the mesh size.

A uniform vertical displacement d_0 was applied at the upper surface of the implant to generate a contact pressure during sliding. The implant was rotated around its central axis up until 20°, with a constant step size of 0.05°. To describe the adhesion and debonding phenomena at the bone-implant interface, a modified Coulomb's law was introduced (Eq. 2) (Immel et al., 2020):

$$\mu(g_s) = \begin{cases} \mu_{ub} & if\ \frac{g_s}{a_s} < 1 \\ \frac{\mu_b+\mu_{ub}}{2} + \frac{\mu_b-\mu_{ub}}{2}\ sin\left(\frac{\pi}{2b_s}\left(\frac{g_s}{a_s} - b_s - 1\right)\right) & if\ 1 \le \frac{g_s}{a_s} \le 1 + 2b_s \\ \mu_b & if\ \frac{g_s}{a_s} > 1 + 2b_s \end{cases} \quad \textbf{(Eq. 2)}$$

where g_s is the sliding distance at the position considered, μ_{ub} and μ_b are the friction coefficients for the unbroken and broken states, respectively, a_s is the sliding threshold up to which tangential adhesion takes effect, and b_s defines the size of the transition zone between the two friction coefficients.

The implant material Ti6Al4V was modelled as linear elastic with Young's modulus E_i = 113 GPa and Poisson's ratio ν_i = 0.3. The bone Poisson's ratio was also defined as ν_b = 0.3. However, the bone Young's modulus E_b, the friction parameters $\{\mu_{ub}, \mu_b, a_s, b_s\}$ and the vertical displacement d_0, were extracted for each specimen based on the experimental data, as described in the following section.

E. Determination of the numerical input parameters from experimental data

First, for each bone-implant sample, the broken friction coefficient μ_b (*i.e.*, when the interface is totally debonded) was determined following Eq. 1 and assuming a homogenous distribution of the normal stress in the contact zone, by using the experimental values of the normal force and torque, averaged for rotation angles ϑ comprised between 10° and 20°. Second, the optimal values of $\{E_b, d_0\}$ were determined following a parametric analysis. For this step, $\{\mu_{ub}, a_s, b_s\}$ were first set equal to {10, 20 µm, 1}, since these parameters do not influence the optimal values of $\{E_b, d_0\}$. E_b was determined by adjusting the initial slope of the numerical torque (ϑ comprised between 0 and 0.3°, which corresponds to a linear evolution of the torque) to the experimental data. The displacement d_0 was chosen so that the induced numerical normal force at the bone-implant interface corresponded to the experimental normal force averaged for values of ϑ comprised between 10° and 20° (tolerance of 0.1 N). Note that the numerical force remained constant during the tests in our model. Third, a minimization procedure was performed to determine $\{\mu_{ub}, a_s, b_s\}$ by comparing the numerical values of the maximal value of the torque T and its corresponding angle ϑ_{max} (with tolerances of 0.005 N.m and 0.05°, respectively) with their corresponding experimental results. Finally, b_s was determined by adjusting the slope of the torque curve for angles between ϑ_{max} and ϑ_{max} + 0.5° (*i.e.,* when the interface starts to debond), minimizing the difference between experimental and numerical torques.

III. Results

A. Friction tests

Figure 2 shows a typical example of the variation of the torque T and of the normal force F as a function of the rotation angle ϑ for a non-integrated implant (see subsection II.c). The torque first increases during the first 4° before stabilizing to a constant value. The normal force decreases also during the first 4°, and continues to decrease with a lower slope between 4° and 15°. The initial decrease of the

force may be due to the fact that during the initial phase, the bone-implant interface is fully bonded and the bone sample is twisted, which results in a decrease of the force due to the effect of the Poisson's ratio. The lower decrease may be due to bone relaxation at the interface. A mean friction coefficient of 0.58 ± 0.057 was obtained when analyzing the results obtained with the 5 friction tests.

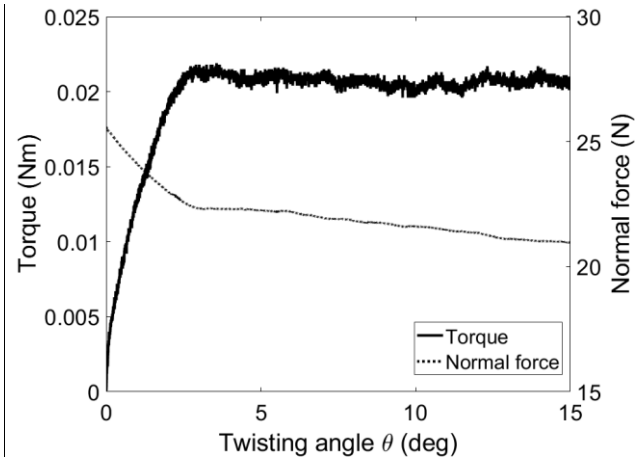

Fig. 2: Evolution of the experimental torque (plain line) and normal force (dotted line) as a function of the twisting angle for a typical friction test.

B. Torque and normal force responses during cleavage tests

The variation of the torque T and of the normal force F as a function of ϑ are qualitatively similar for all specimens (Fig. 3). The torque T first increases almost linearly as a function of ϑ to reach a maximum value (comprised between 0.48 and 0.72 N.m) for $\vartheta = \vartheta_{max}$ = 1.1 ± 0.2° before decreasing to reach a steady value of 0.08 ± 0.017 N.m at around ϑ=10°. A good agreement between the numerical and experimental torques is obtained with some discrepancies shown in Fig. 3 and detailed hereafter. Just before reaching the maximal torque, the slope of the numerical torque is slightly higher than the experimental one. Moreover, the numerical torque approaches its steady final value faster than the experimental data. Experimentally, the normal force increases (from 7-12 N to 31-43 N) during the debonding phase, before stabilizing (difference from the final value < 5%) at an angle equal to 4.2° in average (standard deviation of 1.1°).

The optimized values of the numerical parameters are qualitatively similar for all specimens (Table 1). The friction coefficient is shown to decrease until an average sliding distance of a_s (1 + 2 b_s) = 75.8 µm is reached, which is illustrated by a progressive decrease of the friction coefficient at the bone-implant interface (Fig. 4).

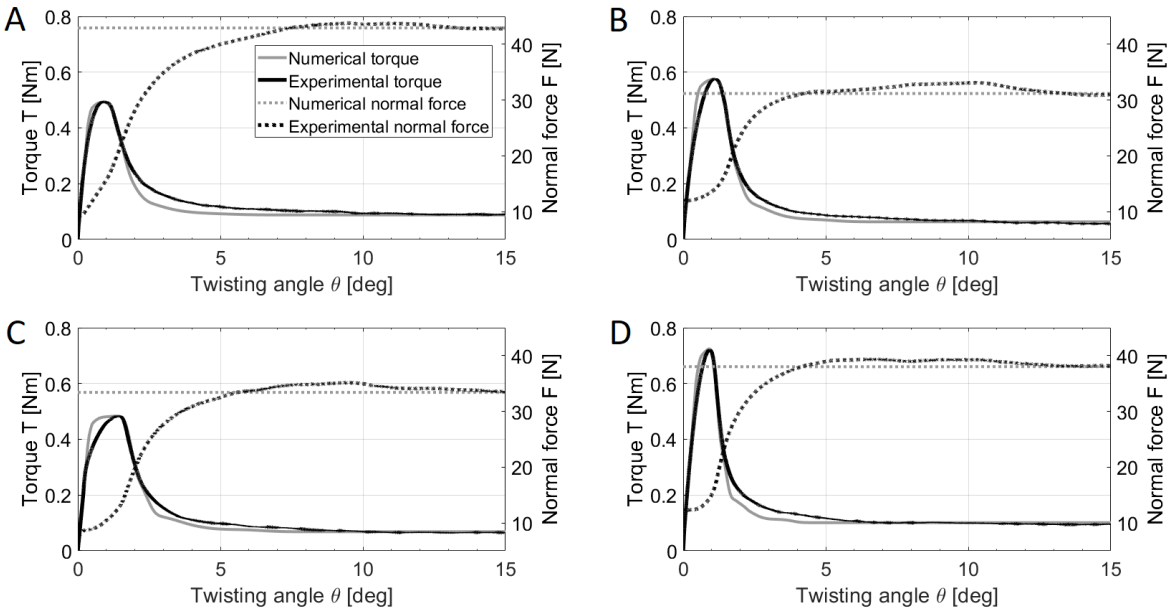

Fig. 3: Variation of the torque (plain lines) and normal force (dashed lines) for experimental (black) and numerical (grey) data as a function of the twisting angle for the four specimens (A to D).

Table 1: Values of the input parameters $\{E_b, d_0, \mu_{ub}, \mu_b, a_s, b_s\}$ for the numerical model, optimized for each of the 4 specimens based on the experimental data.

Sample	E_b (GPa)	d_0 (µm)	μ_{ub}	μ_b	a_s (µm)	b_s
A	35	2.24	6.48	1.15	20	1.4
B	33	1.73	10.28	1.14	24	1.03
C	32	1.91	8.10	1.15	42.5	0.50
D	41	1.71	10.85	1.49	16	1.0
Mean	**35.3**	**1.90**	**8.93**	**1.23**	**25.6**	**0.98**
Standard deviation	**4.03**	**0.25**	**2.02**	**0.17**	**11.7**	**0.37**

C. Numerical debonding of the interface

The variation of the torque T as a function of the rotation angle ϑ depends on the temporal and spatial evolutions of the friction coefficient μ at the bone-implant interface, which is determined locally by the total sliding distance g_s. First, as long as the interface is intact, the torque increases linearly as a function of ϑ up to $\vartheta=\vartheta_s$ (*e.g.*, ϑ_s = 0.4° for sample A, see Fig. 4), while g_s = 0 at the entire implant surface and $\mu = \mu_{ub}$ everywhere as well. Second, for $\vartheta \in [\vartheta_s ; \vartheta_{max}]$, g_s starts to increase, which explains the inflexion of the torque curve. However, since g_s is still lower than a_s for each point of the contact surface, the friction coefficient remains equal to μ_{ub} on the whole surface. Third, when $\vartheta > \vartheta_{max}$ (approximately 1°, when the maximal torque value is reached), g_s is locally higher than a_s, leading to a progressive decrease of the friction coefficient (see Eq. 2) starting at the outer part of the contact surface to its inner part, inducing a decrease of the torque T. Finally, for angles above around 4°, $g_s > a_s (1 + 2b_s)$ on the whole contact surface, the friction coefficient becomes approximately constant and equal to μ_b.

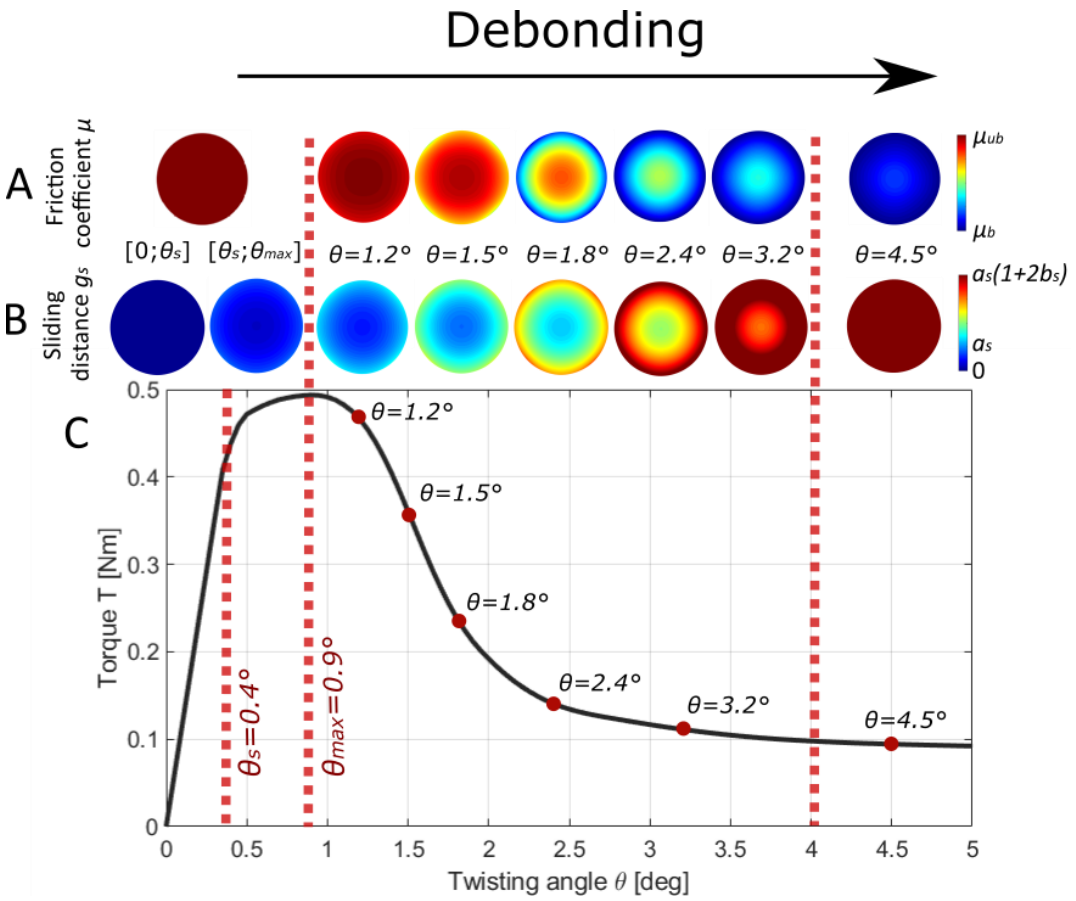

Fig. 4: Illustration of the angular evolution of the friction coefficient μ (A) and of the sliding distance g_s (B) on the contact surface of the coin-shaped implant. The variation of the numerical torque as a function of the twisting angle is shown in (C) for sample #A. The red dotted lines delimit the four regimes describing the debonding of the implant.

D. Experimental estimation of the bone-implant contact

The microscopic images of the stained bone in contact with the implant after the cleavage test revealed qualitatively similar bone coverage for all specimens, with an average BIC ratio of 30% (see Fig. 4).

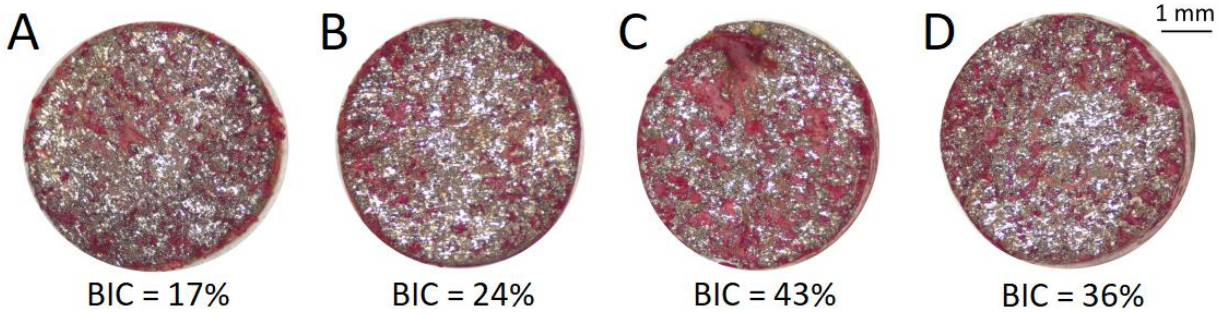

Fig. 5: Microscopic images obtained after the van Gieson picro-fuchsin staining of the contact surface of each implant after testing, with mineralized bone tissue colored in red.

IV. Discussion

Mode III cleavage tests were performed with four osseointegrated coin-shaped implants to provide a better understanding of the debonding of the bone-implant interface subjected to torsional loading. The evolution of the resulting torque and of the normal force were recorded as a function of the rotation angle ϑ and compared to numerical results. The originality of this paper is to provide quantitative information on the mechanical strength of the bone-implant interface through the determination of maximal torques and of friction coefficients. The progressive implants debonding was modeled using an isogeometric finite element model previously developed in (Immel et al., 2020). A good agreement between the experimental and numerical torques was obtained (Fig. 3), which validates that a varying friction coefficient modeling the smooth transition between an unbroken to a broken bone-implant interface can capture its progressive debonding.

A. General behavior during the debonding of osseointegrated implants

Four regimes were evidenced during the debonding of the bone-implant interface, according to the rotation angle ϑ (Fig. 4). For $\vartheta<\vartheta_s$, the torque varies linearly as a function of ϑ since the bone-implant interface is intact ($g_s = 0$), the system being purely elastic. Between ϑ_s and ϑ_{max}, the torque continues to increase, but with a decreasing slope due to low-level sliding occurring on the outer contact zone. However, since g_s remains lower than a_s, the numerical friction coefficient stays maximal ($\mu = \mu_{ub}$ for $g_s < a_s$). For $\vartheta > \vartheta_{max}$, the torque starts to decrease in line with the decrease of the friction coefficient from μ_{ub} to μ_b, thus capturing the transition between adhesion and friction phenomena at the bone-implant interface. Finally, for sufficiently high values of ϑ, the bone-implant interface is completely debonded, which corresponds to a pure friction sliding, where a uniform friction coefficient μ_b is obtained, leading to a constant value of the torque T as a function of ϑ.

A qualitatively similar evolution of the torque as a function of ϑ was obtained experimentally in (Mathieu et al., 2012a). However, higher maximal torque values are obtained herein (approximately 10 times higher), as well as larger differences between the maximal and the final values of the torque (roughly ~87% decrease in the present study compared to 30% in (Mathieu et al., 2012a)). A possible explanation may be related to a higher roughness of the implants used herein (Sa = 24.5 µm compared to Sa = 1.9 µm previously), which may induce higher mechanical interlocking at the bone-implant interface. However, the normal force was not measured in this previous study, and may also have influenced the results, so that a quantitative comparison of the torque values obtained in both studies is difficult.

B. Generation of bone debris at the BII

A significant increase of the normal force was evidenced during the test for all samples, which suggests the presence of bone debris at the interface, generated by the progressive debonding of the bone-implant interface. Due to the confined configuration of the bone-implant interface, the bone debris remained between the two contact surfaces, leading to a dilation of the bone-implant interface and therefore to an increased compressive stress during debonding. This interpretation is reinforced by the steep increase of the normal force starting from ϑ_{max}, *i.e.,* when the bone-implant interface starts to be damaged, before stabilizing, when the bone-implant interface is totally debonded (see Fig. 3). As shown with the five non-osseointegrated implants, (Fig. 2), in absence of osseointegration, the cleavage test described in subsection II.B corresponds to pure friction, without any adhesion. A

significantly lower friction coefficient (average of 0.58 ± 0.057) was obtained (cf. Table 1) compared to osseointegrated samples, which may be explained by the absence of bone debris during the friction tests. Another possible explanation of the higher friction coefficient for osseointegrated samples lies in a possible bone growth on the lateral surfaces of the implants, despite the Teflon protection, which may in turn result in additional friction phenomena. Moreover, the normal force never increased when testing non-osseointegrated implants, which indicates that the increase of F as a function of ϑ is directly related to the bone-implant interface debonding.

C. Influence of the surface roughness, the loading rate and conditions on the friction coefficient

Friction coefficients at the bone-implant interface were found to vary greatly in the literature (Gao et al., 2019; Voutat et al., 2019), with values ranging from 0.14 and 0.73 for titanium implants in contact with human cortical bone (Damm et al., 2015; Yangtao et al., 2008; Yu et al., 2005) and between 0.74 and 1.75 for tantalum implants in contact with cortical bovine bone (Zhang et al., 1999), although all these studies considered non-osseointegrated implants. Multiple factors may influence these variations, such as the implant surface treatment, the normal load, the test conditions, the loading rate, or the lubrication of the bone-implant interface. The results found herein for an osseointegrated and a non-osseointegrated bone-implant interface are in agreement with the results found in the literature. However, due to the influence of these parameters and of the animal model, it is difficult to quantitatively compare the results.

A recent study (Voutat et al., 2019) evidenced that for relatively low values of the compressive stress at the bone-implant interface (values around 30 MPa), the dynamic friction coefficient of the bone-implant interface increases i) when the surface roughness increases (tested up to Ra = 1µm) and ii) when the loading rate decreases (down to 100 µm/sec). In the present study, the tests were performed at even lower compressive stresses (comprised between 1.6 and 2.2 MPa at the bone-implant interface), with rougher implants (Sa = 24.5 µm), and lower loading rate (0.03°/s, which corresponds to 1.31 µm/s on the outer part of the implant). These differences may explain that the friction coefficients (0.58 for non-integrated implants; 1.23 for integrated implants) are in the upper range of the values obtained in (Voutat et al., 2019).

More specifically, a high implant roughness was chosen herein in order to increase the implant stability by introducing strong interlocking phenomena, which generates higher friction coefficients at the bone-implant interface (de Vries et al., 2022). The choice of a low loading rate compared to typical values from the literature (10 µm/s – 10 mm/s) or to the average speed of micromotions induced by walking (around 100 µm/s (Voutat et al., 2019)) was motivated by the necessity to focus on a relatively small range of ϑ, considering that debonding occurs in the first 10° of rotation (see Fig. 3) and that low angles (<1°) are crucial to extract the elastic parameters of an intact bone-implant interface. Furthermore, the numerical model assumes quasi-static displacement. Therefore, a low rotation speed was also necessary to make sure that the numerical and experimental results could be compared as far as practicable.

D. Limitations

The assumptions made to model the contact surfaces may explain the differences between numerical and experimental results (Fig. 3), as well as the high numerical values of E_b (32-41 GPa) compared to

literature values for mature sheep cortical bone (15-32 GPa) (Grant et al., 2014; Spatz et al., 1996). The fully osseointegrated configuration considered numerically does not perfectly represent the experimental contact conditions at the bone-implant interface, since the specimens presented heterogeneous surface roughness and limited BIC ratio (Fig. 5). While the influence of the bone distribution was shown not to significantly impact the resulting torque (Immel et al., 2020), partial contact might still induce a more complex crack front and propagation, which may affect the results. Moreover, introducing a variation of the normal force into the numerical model would also provide a more realistic description of the debonding of the bone-implant interface, considering interlocking phenomena and the possible generation of bone debris. Taking into account bone debris would require updating the loading conditions of the bone-implant interface after each rotation step, which would increase computational complexity and cost.

While newly formed bone tissue is known to be heterogeneous (Manon Fraulob et al., 2020) and viscoelastic (Vayron et al., 2014; Wu et al., 2012), bone tissue was modelled as an isotropic, non-linear elastic, Neo-hookean material, which is still a reasonable assumption in the present case due to the small deformations assumption. Our loading rates are sufficiently small, so that viscoelasticity is not triggered. Moreover, heterogeneities are still captured on average in a homogenized model.

The present study considered a limited number of osseointegrated samples (4), which were similar in terms of surface roughness, healing time and BIC ratio, leading to reproducible results. While considering a single bone-implant interface configuration represents a first step to validate the experimental method and the associated numerical model, future studies should focus on investigating the impact of the variation of the aforementioned biomechanical parameters on the mechanical strength of the bone-implant interface.

Future works will therefore consider different configurations (e.g., healing time and surface roughness) to assess their influence on the implant debonding, and numerical advancements will focus on the integration of a non-homogenous viscoelastic crack propagation.

Conclusions

This study investigates the debonding of coin-shaped implants under torsional loading combining experiments on osseointegrated specimens and simulations considering an isogeometric numerical model. The specimens presented a rough implant surface to enhance mechanical stability, which induced experimentally an increase of the normal force during debonding, suggesting the generation of bone debris during the tests. A good agreement was found between the experiments and the numerical simulations, which validates the assumption that a smooth transition between an unbroken state to a broken state modeled through a varying friction coefficient can be used to simulate the debonding of the bone-implant interface. These results can be utilized in future models of osseointegrated implants.

Acknowledgements

This project has received funding from Paris Ile-de-France Region (DIM “Respore” and F2M Federation), from the CNRS (MITI interdisciplinary program) and from the European Research Council (ERC) under the European Union’s Horizon 2020 research and innovation program (grant agreement

No 682001, project ERC Consolidator Grant 2015 *BoneImplant* and MSCA-IF Bomb Project No 797764). The authors acknowledge the support of the International Research Project (IRP) LAFCUS and the Jülich Aachen Research Alliance Center for Simulation and Data Science (JARA-CSD) School for Simulation and Data Science (SSD).

Conflict of interest statement

The authors indicate that there is no conflict of interest.

References

Berahmani, S., Hendriks, M., Wolfson, D., Wright, A., Janssen, D., Verdonschot, N., 2017. Experimental pre-clinical assessment of the primary stability of two cementless femoral knee components. J Mech Behav Biomed Mater 75, 322–329. https://doi.org/10.1016/j.jmbbm.2017.07.043

Chateauminois, A., Fretigny, C., Olanier, L., 2010. Friction and shear fracture of an adhesive contact under torsion. Phys Rev E Stat Nonlin Soft Matter Phys 81, 026106. https://doi.org/10.1103/PhysRevE.81.026106

Damm, N.B., Morlock, M.M., Bishop, N.E., 2015. Friction coefficient and effective interference at the implant-bone interface. Journal of Biomechanics 48, 3517–3521. https://doi.org/10.1016/j.jbiomech.2015.07.012

de Vries, E., Sánchez, E., Janssen, D., Matthews, D., van der Heide, E., 2022. Predicting friction at the bone – Implant interface in cementless total knee arthroplasty. Journal of the Mechanical Behavior of Biomedical Materials 128, 105103. https://doi.org/10.1016/j.jmbbm.2022.105103

Fraulob, Manon, Le Cann, S., Voumard, B., Yasui, H., Yano, K., Vayron, R., Matsukawa, M., Zysset, P., Haïat, G., 2020. Multimodal Evaluation of the Spatio-Temporal Variations of Periprosthetic Bone Properties. J Biomech Eng. https://doi.org/10.1115/1.4048399

Fraulob, M, Vayron, R., Le Cann, S., Lecuelle, B., Hériveaux, Y., Albini Lomami, H., Flouzat Lachaniette, C.H., Haïat, G., 2020. Quantitative ultrasound assessment of the influence of roughness and healing time on osseointegration. Sci Rep 10.

Galloway, F., Kahnt, M., Ramm, H., Worsley, P., Zachow, S., Nair, P., Taylor, M., 2013. A large scale finite element study of a cementless osseointegrated tibial tray. Journal of Biomechanics 46, 1900–1906. https://doi.org/10.1016/j.jbiomech.2013.04.021

Gao, X., Fraulob, M., Haïat, G., 2019. Biomechanical behaviours of the bone–implant interface: a review. J. R. Soc. Interface 16, 20190259. https://doi.org/10.1098/rsif.2019.0259

Grant, C.A., Wilson, L.J., Langton, C., Epari, D., 2014. Comparison of mechanical and ultrasound elastic modulus of ovine tibial cortical bone. Med Eng Phys 36, 869–874. https://doi.org/10.1016/j.medengphy.2014.03.012

Guillaume, F., Le Cann, S., Tengattini, A., Törnquist, E., Falentin-Daudre, C., Albini Lomami, H., Petit, Y., Isaksson, H., Haïat, G., 2021. Neutron microtomography to investigate the bone-implant interface – Comparison with histological analysis. Phys Med Biol. https://doi.org/10.1088/1361-6560/abf603

Haïat, G., Wang, H.-L., Brunski, J., 2014. Effects of biomechanical properties of the bone-implant interface on dental implant stability: from in silico approaches to the patient's mouth. Annu Rev Biomed Eng 16, 187–213. https://doi.org/10.1146/annurev-bioeng-071813-104854

I-Chiang, C., Shyh-Yuan, L., Ming-Chang, W., Sun, C.-W., Jiang, C.-P., 2014. Finite element modelling of implant designs and cortical bone thickness on stress distribution in maxillary type IV bone. Comput Methods Biomech Biomed Engin 17, 516–526. https://doi.org/10.1080/10255842.2012.697556

Immel, K., Duong, T.X., Nguyen, V.-H., Haïat, G., Sauer, R.A., 2020. A modified Coulomb's law for the tangential debonding of osseointegrated implants. Biomech Model Mechanobiol 19, 1091–1108. https://doi.org/10.1007/s10237-019-01272-9

Kurniawan, D., Nor, F.M., Lee, H.Y., Lim, J.Y., 2012. Finite element analysis of bone-implant biomechanics: refinement through featuring various osseointegration conditions. Int J Oral Maxillofac Surg 41, 1090–1096. https://doi.org/10.1016/j.ijom.2011.12.026

Mathieu, V., Vayron, R., Barthel, E., Dalmas, D., Soffer, E., Anagnostou, F., Haiat, G., 2012a. Mode III cleavage of a coin-shaped titanium implant in bone: effect of friction and crack propagation. J Mech Behav Biomed Mater 8, 194–203. https://doi.org/10.1016/j.jmbbm.2011.12.012

Mathieu, V., Vayron, R., Soffer, E., Anagnostou, F., Haïat, G., 2012b. Influence of healing time on the ultrasonic response of the bone-implant interface. Ultrasound Med Biol 38, 611–618. https://doi.org/10.1016/j.ultrasmedbio.2011.12.014

Mathieu, Vayron, Richard, Lambert, Naili, Meningaud, Haiat, 2014. Biomechanical determinants of the stability of dental implants: Influence of the bone–implant interface properties. Journal of Biomechanics 47, 3–13. https://doi.org/10.1016/j.jbiomech.2013.09.021

Mondal, S., Ghosh, R., 2019. Effects of implant orientation and implant material on tibia bone strain, implant-bone micromotion, contact pressure, and wear depth due to total ankle replacement. Proc Inst Mech Eng H 233, 318–331. https://doi.org/10.1177/0954411918823811

Oliscovicz, N., Shimano, A., Marcantonio, E., Lepri, C., Reis, A., 2013. Analysis of Primary Stability of Dental Implants Inserted in Different Substrates Using the Pullout Test and Insertion Torque. International journal of dentistry 2013, 194987. https://doi.org/10.1155/2013/194987

Rice, J.R., Ruina, A.L., 1983. Stability of Steady Frictional Slipping. Journal of Applied Mechanics 50, 343–349. https://doi.org/10.1115/1.3167042

Rønold, H.J., Ellingsen, J.E., 2002. The use of a coin shaped implant for direct in situ measurement of attachment strength for osseointegrating biomaterial surfaces. Biomaterials 23, 2201–2209. https://doi.org/10.1016/s0142-9612(01)00353-2

Rønold, H.J., Lyngstadaas, S.P., Ellingsen, J.E., 2003. Analysing the optimal value for titanium implant roughness in bone attachment using a tensile test. Biomaterials 24, 4559–4564. https://doi.org/10.1016/S0142-9612(03)00256-4

Ruina, A., 1983. Slip instability and state variable friction laws. Journal of Geophysical Research: Solid Earth 88, 10359–10370. https://doi.org/10.1029/JB088iB12p10359

Seong, W.J., Grami, S., Jeong, S.C., Conrad, H.J., Hodges, J.S., 2013. Comparison of Push-In versus Pull-Out Tests on Bone-Implant Interfaces of Rabbit Tibia Dental Implant Healing Model. Clinical Implant Dentistry and Related Research 15, 460–469. https://doi.org/10.1111/j.1708-8208.2011.00357.x

Shirazi-Adl, A., 1992. Finite element stress analysis of a push-out test. Part 1: Fixed interface using stress compatible elements. J Biomech Eng 114, 111–118. https://doi.org/10.1115/1.2895434

Shirazi-Adl, A., Dammak, M., Paiement, G., 1993. Experimental determination of friction characteristics at the trabecular bone/porous-coated metal interface in cementless implants. J Biomed Mater Res 27, 167–175. https://doi.org/10.1002/jbm.820270205

Spatz, H.C., O'Leary, E.J., Vincent, J.F., 1996. Young's moduli and shear moduli in cortical bone. Proc Biol Sci 263, 287–294. https://doi.org/10.1098/rspb.1996.0044

Tschegg, E.K., Lindtner, R.A., Doblhoff-Dier, V., Stanzl-Tschegg, S.E., Holzlechner, G., Castellani, C., Imwinkelried, T., Weinberg, A., 2011. Characterization methods of bone-implant-interfaces of bioresorbable and titanium implants by fracture mechanical means. J Mech Behav Biomed Mater 4, 766–775. https://doi.org/10.1016/j.jmbbm.2010.08.004

Vayron, R., Matsukawa, M., Tsubota, R., Mathieu, V., Barthel, E., Haiat, G., 2014. Evolution of bone biomechanical properties at the micrometer scale around titanium implant as a function of healing time. Phys Med Biol 59, 1389–1406. https://doi.org/10.1088/0031-9155/59/6/1389

Vayron, R., Nguyen, V.-H., Lecuelle, B., Albini Lomami, H., Meningaud, J.-P., Bosc, R., Haiat, G., 2018. Comparison of Resonance Frequency Analysis and of Quantitative Ultrasound to Assess Dental Implant Osseointegration. Sensors (Basel) 18. https://doi.org/10.3390/s18051397

Voutat, C., Nohava, J., Wandel, J., Zysset, P., 2019. The Dynamic Friction Coefficient of the Wet Bone-Implant Interface: Influence of Load, Speed, Material and Surface Finish. Biotribology 17. https://doi.org/10.1016/j.biotri.2019.03.002

Wu, Z., Ovaert, T.C., Niebur, G.L., 2012. Viscoelastic properties of human cortical bone tissue depend on gender and elastic modulus. J Orthop Res 30, 693–699. https://doi.org/10.1002/jor.22001

Yangtao, X., Yan, Y., Tiandong, X., 2008. Study on Fretting Friction Coefficient between NiTi Shape Memory Alloy and Human Bone in Hank's Solution. Rare Metal Materials and Engineering 37, 1201–1205. https://doi.org/10.1016/S1875-5372(09)60032-1

Yu, H.Y., Cai, Z.B., Zhou, Z.R., Zhu, M.H., 2005. Fretting behavior of cortical bone against titanium and its alloy. Wear, 15th International Conference on Wear of Materials 259, 910–918. https://doi.org/10.1016/j.wear.2005.01.037

Zhang, Y., Ahn, P.B., Fitzpatrick, D.C., Heiner, A.D., Poggie, R.A., Brown, T.D., 1999. INTERFACIAL FRICTIONAL BEHAVIOR: CANCELLOUS BONE, CORTICAL BONE, AND A NOVEL POROUS TANTALUM BIOMATERIAL. J. Musculoskelet. Res. 03, 245–251. https://doi.org/10.1142/S0218957799000269